Oscillation Damping of Integrated Transmission and Distribution Power Grid With Renewables Based on Novel Measurement-Based Optimal Controller

Olalekan Ogundairo, *Student Member, IEEE*, Sukumar Kamalasadan, *Senior Member, IEEE*, Anuprabha R. Nair, *Student Member, IEEE*, and Michael Smith, *Member, IEEE*

***Abstract*—Renewable energy resources are gaining fast adoption in the power grid because of their relatively low cost and offered environmental benefits. However, the grid will experience decreased inertia as a result of these added resources. Numerous research studies have focused on improving the grid damping, including the lack of inertia, due to renewable resource integration. In this article, we present an adaptive damping controller to help mitigate oscillations during disturbances on the grid, caused by fault occurrences, sudden load changes, capacitor switching, or even the intermittent nature of the energy sources for most renewable systems, considering both integrated transmission and distribution systems. The test system is developed based on Kundur's two-area system as the transmission system and the IEEE 123-bus system as the distribution system. Then, the novel proposed adaptive optimal damping control architecture is validated via simulation-based test cases conducted in MATLAB/Simulink using real-life grid data. It is observed that the proposed control architecture not only damps the oscillations more than 10% as compared with the state-of-the-art methods but can also control multiple generators.**

***Index Terms*—Distributed energy resource (DER), doubly fed induction generator (DFIG), integrated T&D system, optimal damping controller, synchronous generator.**

NOMENCLATURE

ψ_{qs}	Stator flux.
A	Exponential zone amplitude (V).
C	Capacitance of the dc converter.
C_{in}	Input capacitance.
C_{out}	Output capacitance.
D	Duty cycle input of the converter.
E_0	Battery voltage constant (V).
F_{HP}	Flow high pressure.
F_{LP}	Flow low pressure.
H	Inertia.
i	Battery current (A).
i^*	Filtered current (A).
$i_{d/q}$	d- and q-axis inverter output current.
K	Polarization constant (V/Ah).
$k^L_{\text{PSS},i}$	Lower bound value of the PSS gain.
$k^U_{\text{PSS},i}$	Upper bound value of the PSS gain.
K_a	Exciter gain.
K_f	Stabilizer gain.
K_{PSS}	PSS gains.
L	Inductance of the dc converter.
L_{inv}	Inverter inductance.
L_{in}	Filter input inductance.
L_{rr}	Exciter gain.
P_{disch}	Rotor resistance.
P_{CH}	Position of chest delay.
r_r	Rotor inductance.
P_{CO}	Position of crossover.
P_{batt}	Rotor resistance.
P_{GV}	Position of governor value.
P_{RH}	Position of reheater.
R	Internal resistance of the battery.
P_{ch}	Rotor inductance.
T_ω	Wash filter time constant.
T_{CH}	Chest delay time constants.
T_{CO}	Crossover delay time constants.
T_{SM}	Reference of voltage.
T_{SR}	Reference of voltage.
V_{bat}	Internal battery voltage (V).
$V_{d/q}$	d- and q-axis inverter output voltage.
V_{dc}	voltage at dc link.
V_{dl}	d-axis voltages across the inverter L_{inv}.
V_f	Stabilizer EMF.
V_{pcc}	Voltage at the PCC.
V_{pss}	Output reference of the power system stabilizer.
V_{ql}	q-axis voltages across the inverter L_{inv}.
V_{ref}	Reference of voltage.
V_r	Input filter EMF.
$i_{d/q}$	d- and q-axis grid current.

Manuscript received December 31, 2021; revised March 15, 2022; accepted March 18, 2022. Date of publication March 29, 2022; date of current version May 20, 2022. Paper 2021-IACC-1427.R1, presented at the 2020 IEEE International Conference on Power Electronics, Drives and Energy Systems, Jaipur, India, Dec. 16–19, and approved for publication in the IEEE TRANSACTIONS ON INDUSTRY APPLICATIONS by the Industrial Automation and Control Committee of the IEEE Industry Applications Society. This work was supported in part by the National Science Foundation under Grant ECS-1810174 awarded to Sukumar Kamalasadan. *(Corresponding author: Sukumar Kamalasadan.)*

The authors are with the Energy Production Infrastructure Center, Department of Electrical Engineering, and Department of Engineering Technology and Construction Management, University of North Carolina at Charlotte, Charlotte, NC 28223 USA (e-mail: oogundai@uncc.edu; skamalas@uncc.edu; anair8@uncc.edu; michael.smith@uncc.edu).

Color versions of one or more figures in this article are available at https://doi.org/10.1109/TIA.2022.3162565.

Digital Object Identifier 10.1109/TIA.2022.3162565

$i_{ds/r}$ Stator- and rotor-side current d-frame.
$i_{qs/r}$ Stator- and rotor-side current q-frame.
$V_{d/q}$ d- and q-axis grid voltages.
$V_{d1/q1}$ d- and q-axis output voltages of the inverter.
$V_{ds/r}$ Stator- and rotor-side voltage d-frame.
$V_{qs/r}$ Stator- and rotor-side voltage q-frame.

I. Introduction

RECENT trends in electricity generation include the interconnection of several resources with the traditional power grid. Among the new resources, renewable energy resources (RERs) are gaining fast adoption because of their offered economic, environmental, and sustainability benefits. In addition, many policies are major drivers for the adoption of RERs [1], [2]. The electricity delivery frequency determines the point of interconnection for these resources, depending on the type of RER. For instance, wind turbines are connected to the transmission layer. At the same time, small-scale or residential solar systems can be connected to the distribution layer, which can be referred to as distributed generation (DG). Studies show there are 12 million DG units across the U.S. with a total capacity of 200 GW [3]. RERs can be operated in both a grid-connected mode and an off-grid mode. In a grid-connected mode, the traditional grid is transformed from a unidirectional flow into a bidirectional flow, which increases the network complexity. In most RERs, power generation varies due to the intermittency/variability of the source. For example, wind speed variability results in wind turbine frequency and power output fluctuations [4]. This variability can have a significant impact on the grid. These impacts can be more severe, depending on the level of renewable energy penetration. Some of these impacts result in the violation of power quality standards, such as the voltage ANSI value (0.95–1.05 p.u.) or the frequency, which should be kept between 59.5 and 60.5 Hz; therefore, the system does not lose stability. Power quality is assumed to be good if the aforementioned metrics remain at an acceptable steady value of voltages and frequency, with a smooth sinusoidal waveform. This showcases the need for effective control and management strategies.

Battery energy storage devices are one of the approaches that have been widely implemented for load frequency control [5]. Batteries are also being used for the smoothing of RERs, which can be connected to the dc link of solar photovoltaics (PVs) or the dc-link capacitance of a wind turbine. Despite the advantages of the interconnection of batteries by charging and discharging, the fast-changing behavior of ambient sources and the capacity of the battery play a major role in addressing these issues. During the short-circuit condition that occurs while connecting networks, fixed wind speeds can also result in instability because of the high level of reactive power that is absorbed. Other methods to mitigate frequency fluctuation include superconductive magnetic energy storage systems. Despite the advantages of higher long life and density, this solution is quite expensive to implement. Lack of inertia is another major challenge with the interconnection of these resources and the reason that they are susceptible to frequency fluctuations.

In terms of power generation, wind energy is harvested using wind energy conversion systems (WECSs). Unlike conventional plants that use synchronous generators, a WECS uses different generators, such as squirrel cage induction, doubly fed induction, and permanent magnet synchronous generators. A doubly fed induction generator (DFIG) offers improved performance concerning the variability of wind sources, leading to minimized power losses. It also provides generation system improvements over other WECSs. Furthermore, DFIGs have several benefits for use with variable-speed wind turbines, such as high energy efficiency and controllability [6]. To control DFIG-based generation in both the grid-connected and islanded modes of operation, several different control techniques have previously been implemented. For example, a cycloconverter-based control approach was proposed in [7] for the decoupled control of DFIG active and reactive power. To analyze the relation between the frequency and impedance of compensation networks, some studies have been based on frequency scanning methods [8]. Grid-connected optimization and control approaches for supporting the grid both with and without batteries to provide additional stability improvement are reported in [9]–[12]. For grid ancillary support, a battery energy storage system (BESS) with advanced control management is key [13]. In some studies, to improve power quality, the BESS is integrated with the V_{dc} link of the pulsewidth modulation back-to-back converters. However, the main disadvantage associated with these control architectures is that they cannot adaptively damp the frequency oscillations.

Power system stabilizers (PSSs) are overviewed as supplementary controllers to damp system oscillations. The highly nonlinear and dynamic nature of the power grid impacts the performance of conventional PSSs. Hence, some advanced PSS control architectures based on adaptive neural and fuzzy-based control logic have been discussed by many researchers. An adaptive neuro-fuzzy-based adaptive PSS control is discussed in [14]. The dynamic behavior of the plant is identified, and the input link weights of the neural network are adaptively adjusted. While a conventional PSS uses generator speed as the local power signal to damp the oscillations, the idea of improving the observability of the PSS by employing an additional signal is discussed in [15]. A similar approach of a modified PSS to effectively damp the oscillations is presented in [16] and [17]. While Zhao and Malik [16] make use of a recursive gradient algorithm for the adaptive PSS design, the architecture in [17] is based on an inherent deadband adaptive tune architecture, which can track the system operating modes without any strict prerequisites, as demanded by most architectures. The advantages of adaptive and dynamic controllers to improve the overall performances of nonlinear systems, including the power grid, are reported in [15] and [18]–[23]. Many of these adaptive architectures require large disturbances for the training of the control architecture and may often experience convergence problems. Hence, it demands the need for a computationally less complex adaptive architecture that dynamically adjusts itself with the nonlinear nature of the power grid to efficiently damp the oscillations. In our earlier works, we have demonstrated the ability of adaptive controllers for controlling nonlinear systems [24]–[27]. Furthermore, an adaptive online damping controller for the grid-side converter

(GSC) for battery-integrated wind farms is presented in our previous work [28].

In this article, a novel adaptive online PSS based on the optimization of a linear–quadratic cost function is proposed. The PSS gains are dynamically adjusted based on the minimization of generator speed variations. The objective of this study is to develop a more effective damping controller that can be used for operations with different system architectures, especially integrated transmission and distribution (T&D) systems, with distributed energy resources (DERs) varying from the distribution side and having significant effects on the transmission network parameters. In addition, the controller has damping capabilities for frequency and voltage oscillations, and the proposed controller can be used to minimize the effects of harmonic loads. The proposed controller's performance is evaluated for several simulation-based test cases (e.g., load dynamics, faults, and varying wind speeds). The major contributions of this article compared to the state of the art are as follows.

1) An adaptive damping controller is proposed that can damp oscillations in multiple generators considering variations in both the T&D power grids that include RERs.
2) The proposed architecture is based on an optimal control theory; therefore, multiple devices can be controlled with this damping control architecture.
3) The approach uses resources considering both the centralized and distributed generators in both the T&D systems.
4) The performance of the proposed control architecture is superior during dynamic grid conditions, as compared with the performance of a conventional approach, because of its adaptive tuning capability, and the approach is field implementable.

Moreover, compared to earlier work in [28], the advantages of the proposed work include the following.

1) An optimal damping controller can augment generator controllers and/or PSS, which can effectively damp the oscillations in T&D networks.
2) The architecture can dynamically adjust the gain values based on linear optimization that modulates the generator excitation to effectively damp the oscillations.
3) Unlike the previous work, which relies on active power modulation from a DFIG and additional power from a battery for damping, the proposed work can efficiently coordinate the generators, thereby efficiently utilizing the available power from nearby generators to damp the oscillations under dynamic grid conditions.

The rest of this article is organized a follows. Section II describes the design and modeling of the associated energy sources. Section III details the proposed frequency damping controller. Section IV provides the validation test cases and discusses the results. Finally, Section V concludes this article.

II. Design and Modeling of Energy Sources

The modeling and design of the four main energy sources used in the test system are discussed in this section. It includes synchronous generators, a DFIG, an ac microgrid, and a battery system. The network architecture is designed to simulate an interconnection of a T&D network. The transmission system is a Kundur two-area network, with a wind turbine connected at the tie-lines, while the distribution network is an IEEE 123-bus system, which has a solar PV connected to one of its buses.

A. Synchronous Generators

The test system has four synchronous generators types: one slack generator (V, δ control) and three PV generators (P, V control). All the generators are represented using synchronous generator models, rather than voltage sources, to effectively demonstrate the generator dynamics. The synchronous generators are connected to the transmission system, modified from a Kundur two-area system. Area 1 has one slack generator and one PV bus generator, while Area 2 has two PV bus generators. In the synchronous generator architecture, the steam turbine governor is used to control active power, while excitation control is used for voltage management. The steam turbine governor is used to control the active power through the speed and frequency of the generator. In addition, the exciter is used to control the grid voltage

$$\frac{d}{dt}\begin{bmatrix}\Delta\omega_r\\ \Delta P_{\rm SR}\\ \Delta P_{\rm GV}\\ \Delta P_{\rm CH}\\ \Delta P_{\rm RH}\\ \Delta P_{\rm CO}\end{bmatrix}=\begin{bmatrix}\frac{-K_D}{T_{\rm SR}} & 0 & 0 & \frac{F_{\rm HP}}{2H} & \frac{F_{\rm IP}}{2H} & \frac{F_{\rm LP}}{2H}\\ \frac{-K_{\rm GS}}{T_{\rm SR}} & 0 & 0 & 0 & 0 & 0\\ 0 & \frac{1}{T_{\rm SM}} & \frac{-1}{T_{\rm SM}} & 0 & 0 & 0\\ 0 & 0 & \frac{1}{T_{\rm CH}} & \frac{-1}{T_{\rm CH}} & 0 & 0\\ 0 & 0 & 0 & \frac{1}{T_{\rm RH}} & \frac{-1}{T_{\rm RH}} & 0\\ 0 & 0 & 0 & 0 & \frac{1}{T_{CO}} & \frac{-1}{T_{CO}}\end{bmatrix}\begin{bmatrix}\Delta\omega_r\\ \Delta P_{\rm SR}\\ \Delta P_{\rm GV}\\ \Delta P_{\rm CH}\\ \Delta P_{\rm RH}\\ \Delta P_{\rm CO}\end{bmatrix}+\begin{bmatrix}0 & \frac{-1}{2H}\\ \frac{1}{T_{\rm SR}} & 0\\ 0 & 0\\ 0 & 0\\ 0 & 0\\ 0 & 0\end{bmatrix}\begin{bmatrix}\Delta P_{\rm ref}\\ \Delta P_L\end{bmatrix}. \tag{1}$$

For the synchronous generators, the steam turbine governor control ensures the stability of the power reference. The field voltage reference for the generator is provided by the excitation controller. In addition, a voltage stabilizer is used to improve the grid voltage in accordance with IEEE-DC4B and IEEE-STIA. The synchronous generator dynamic equations are in (1)–(4)

$$V_f = k_A(V_{\rm ref}+V_{\rm pss}-V_r)$$
$$V_{f\min}\le V_f\le V_{f\max} \tag{2}$$
$$\frac{V_{f\min}}{K_a}\le V_{\rm PID}\le\frac{V_{f\max}}{K_a} \tag{3}$$
$$V_{\rm PID}-\left(V_{\rm ref}+V_{\rm pss}-V_t-\frac{K_f}{T_f}[V_f-V_{\rm stab}]\right). \tag{4}$$

$V_{\rm ref}$ is the reference voltage, K_a is the exciter gain, V_f is the stabilizer EMF, $V_{\rm stab}$ is the stabilizer voltage, $V_{\rm pss}$ is the output reference of the PSS, K_f is the stabilizer gain, and V_r is the input filter EMF.

B. DFIG Model

The voltage equations of the DFIG in the synchronous rotating (dq frame) model are described as follows:

$$v_{qs} = -r_s i_{qs} + \omega_e \psi_{ds} + p\psi_{qs} \tag{5}$$

$$v_{ds} = -r_s i_{ds} + \omega_e \psi_{qs} + p\psi_{ds} \tag{6}$$

$$v_{qr} = -r_r i_{qr} + (\omega_e - \omega_r)\psi_{dr} + p\psi_{qr} \tag{7}$$

$$v_{dr} = -r_r i_{dr} + (\omega_e - \omega_r)\psi_{qr} + p\psi_{dr} \tag{8}$$

where $v_{ds/r}$, $i_{ds/r}$ and $v_{qs/r}$, $i_{qs/r}$ are the stator- and rotor-side voltage and current in the dq frame, respectively.

1) Grid-Side Converter: The GSC is used to maintain constant DC-link voltage and to regulate reactive power supplied to the grid. This is accomplished via the use of stator voltage-oriented control. For control of the reactive power, the stator voltage d-axis component is aligned with the stator voltage, whereas the q-axis component is set to 0. The GSC $d-q$ frame control equation is detailed as follows.

$$\begin{bmatrix} v_d \\ v_q \end{bmatrix} = R \begin{bmatrix} i_d \\ i_q \end{bmatrix} + L\rho \begin{bmatrix} i_d \\ i_q \end{bmatrix} + Lw_e \begin{bmatrix} -i_q \\ i_d \end{bmatrix} + \begin{bmatrix} v_{d1} \\ v_{q1} \end{bmatrix} \tag{9}$$

The GSC controller active and reactive power are shown as,

$$\begin{bmatrix} P \\ Q \end{bmatrix} = \begin{bmatrix} v_q i_q \\ v_q i_d \end{bmatrix} \tag{10}$$

where i_d and i_q are the $d-q$ axis currents from the inverter, v_d and v_q are the $d-q$ axis grid voltages, and v_{d1} and v_{q1} are the $d-q$ axis output voltages of the inverter.

2) Rotor-Side Converter (RSC): The RSC's main objective is to ensure that the machine operates at maximum power point tracking (MPPT), even during varying wind speeds, by controlling the speed of the turbine. The RSC also ensures that the active power and reactive power track to their respective reference values by controlling the excitation voltage. A stator flux-oriented frame ($\psi_{qs} = 0$, $v_{qs} = v_s$) is used with the vector control of the RSC. The active power and reactive power of the stator are expressed as a function of the rotor current as

$$P_s = v_{qs} * \frac{L_m}{L_{rr}} i_{qr} \tag{11}$$

$$Q_s = v_{qs} * \frac{L_m}{L_{rr}} i_{qr} + \psi_{ds} \tag{12}$$

with rotor voltage represented as

$$v_{qr} = v_{qr}^* + (\omega_e - \omega_r)\left(\sigma L_{rr} i_{dr} + \frac{L_m}{L_s}\psi_{ds}\right) \tag{13}$$

$$v_{dr} = v_{dr}^* - (\omega_e - \omega_r)(\sigma L_{rr} i_{qr}) \tag{14}$$

where L_{rr} and r_r represents the rotor inductance and resistance and $\sigma = 1 - \frac{L_m^2}{L_s L_r}$.

C. RER-Integrated Power Distribution System

A large RER is connected to the distribution system, IEEE 123-bus system, where the RER is comprised of a PV farm, battery, and inverter system, as shown in Fig. 1. The details of the system parameters are included in Table V. The PV farm is located at bus 48. The PV penetration level capacity is provided in Table I. The RER also has a battery system connected to the dc-link bus, which is interconnected with an ac inverter.

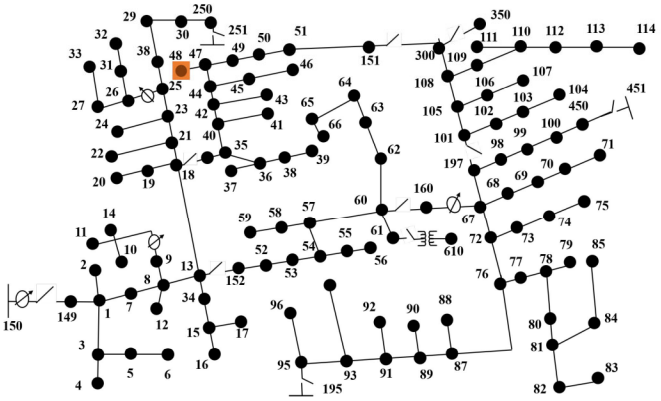

Fig. 1. PV and load areas in the IEEE 123-bus system.

TABLE I
LOCATION AND RATING OF DERS IN THE IEEE 123-BUS SYSTEM

PV Rating	BESS Rating	NodeIDs
2MVA	1.2MWh	48

1) PV Farm: The PV system generates 2 MW at the maximum power of operation. The system comprises several solar panels and controllers, such as MPPT to ensure that maximum power is obtained from the resources. The point of common coupling (PCC), which can be referred to as the dc link, has dc power connected to the inverter. The state-space representation of the PV system is shown as follows:

$$\begin{bmatrix} \dot{\bar{i}} \\ \dot{\bar{V}} \end{bmatrix} = \begin{bmatrix} 0 & \frac{-D}{L} \\ \frac{-D}{C} & \frac{-1}{RC} \end{bmatrix} \begin{bmatrix} \bar{i} \\ \bar{V} \end{bmatrix} + \begin{bmatrix} \frac{1}{L} & 0 & \frac{V}{L} \\ 0 & \frac{-1}{C} & \frac{i}{C} \end{bmatrix} \begin{bmatrix} \overline{V_{\text{pv}}} \\ \overline{i_o} \\ \overline{D_{\text{mpp}}} \end{bmatrix} \tag{15}$$

$$\begin{bmatrix} V \\ i \end{bmatrix} = \begin{bmatrix} 0 & 1 \\ 1 & 0 \end{bmatrix} \begin{bmatrix} \bar{i} \\ \bar{V} \end{bmatrix}. \tag{16}$$

In these equations, V_{pv} is the input-side voltage, i_o is the output-side current, and L, C, and D are the inductance, capacitance, and the duty cycle for the buck operation of the converter. D_{mpp} is the duty cycle input to the converter for boost operation. In addition, i, V_g, and V are the inductor current, input voltage, and output voltage, respectively.

2) Battery Model: The battery control system is similar to that of the PV system. The major difference is that, unlike the PV system that does not include a buck mode of operation, the battery can operate in both the buck and boost modes for its converter, which depends on the battery mode (i.e., in a mode of discharging or charging). The battery is also responsible for maintaining the dc-link voltage. The battery control system functions as follows. The dc-link voltage, which is maintained as a constant, is measured. However, the current flowing through the battery varies. This results in the battery operation mode changing to either charging or discharging, accordingly. The filter parameters for the battery (e.g., inductance L_{in}, input capacitance C_{in}, and output capacitance C_{out}) are included in the

design. The controller, implemented as two cascaded controllers, provides function in a buck–boost operation mode. The inner loop controls the current and provides the duty cycle reference for the generating switching pulses, whereas the outer loop control maintains a constant V_{dc} value. The battery voltage can be represented as

$$V_{\text{bat}} = E_o - K\frac{Q}{Q-it}it - Ri + Ae^{-B\int idt} - K\frac{Q}{Q-it}i^* \tag{17}$$

where V_{bat} is the internal battery voltage (V), E_0 is the battery voltage constant (V), K is the polarization constant (V/Ah), K is the polarization constant (V/Ah), battery capacity (Ah), A is the exponential zone amplitude (V), R is the internal resistance of the battery, $\int idt$ is the actual battery charge (Ah), i is the battery current (A), and i^* is filtered current (A).

The transfer function for the dc–dc converter is given by

$$\frac{I_i}{d} = \frac{S\frac{V_o}{L} + \frac{V_o}{RLC} + \frac{I_L D'}{LC}}{S^2 + \frac{1}{RC}S - \frac{D^2}{LC}} \tag{18}$$

$$P_{\text{batt}} = \begin{cases} P_{\text{disch}}, & V_{\text{pcc}} < 1 \\ 0, & V_{\text{pcc}} = 1 \\ P_{\text{ch}}, & V_{\text{pcc}} > 1 \end{cases} \tag{19}$$

where P_{batt} is the status of the battery, P_{disch} indicates discharging, and P_{ch} represents charging.

3) Inverter Model: The inverter type has an L filter, referred to as L inverter, where the dq equations guiding its operations are as follows:

$$V_{dl} = L_{\text{inv}}\frac{di_d}{dt} - wL_{\text{inv}}i_q + V_d \tag{20}$$

$$V_{ql} = L_{\text{inv}}\frac{di_q}{dt} - wL_{\text{inv}}i_d + V_q \tag{21}$$

where V_{dl} and V_{ql} are d- and q-axis voltages across inductor L_{inv}, respectively; ω is the supply voltage angular frequency, L is the inductance of the L-type filter; and i_d, i_q and V_d, V_q are the d- and q-axis inverter output current and voltages, respectively. The active and reactive power outputs when connected to the grid are given by

$$P = V_d i_d \tag{22}$$

$$Q = V_q i_q. \tag{23}$$

The state-space representation of the inverter equation in a grid-connected mode is shown below. If V_d (grid voltage) is kept constant, then i_d and i_q can be used to control the active and reactive power

$$\begin{bmatrix} i_d \\ i_q \end{bmatrix} = \begin{bmatrix} 0 & \omega \\ \omega & 0 \end{bmatrix}\begin{bmatrix} i_d \\ i_q \end{bmatrix} + \begin{bmatrix} \frac{1}{L_{\text{inv}}} & 0 \\ 0 & \frac{1}{L_{\text{inv}}} \end{bmatrix}\begin{bmatrix} (V_{dl} - V_d) \\ (V_{ql} - V_q) \end{bmatrix} \tag{24}$$

$$\begin{bmatrix} P_{ac} \\ Q_{ac} \end{bmatrix} = \begin{bmatrix} V_d & V_q \\ -V_q & V_d \end{bmatrix}\begin{bmatrix} i_d \\ i_q \end{bmatrix}. \tag{25}$$

The optimal controllers are integrated with the PSS for each of the synchronous generators, as discussed in Section III.

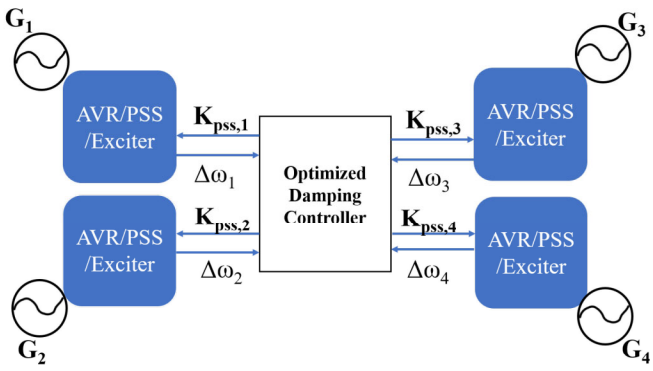

Fig. 2. Schematic of the proposed controller with generators.

III. Proposed Optimal Damping Controller

The proposed optimal damping controller architecture is shown in Fig. 2, and the field implementation framework is illustrated in Fig. 3. The feedback-based proposed supplementary damping control loop is implemented considering the frequency deviations measured on the grid at the tie-line between Areas 1 and 2.

A. Mathematical Model of the Proposed Controller

Considering the power grid models designed in Section II. A finite horizon optimal control framework can be developed if we have a model that relates to a state-space representation of the system as $x_{k+1} = Ax_k + BU_k$.

With the system model in state space, we can define an optimal control framework by minimizing

$$J_{\text{obj}} = \frac{1}{2}\sum_{k=0}^{N}\left[(x_k)^T Q_c x_k + (u_k)^T R_c U_k\right] \tag{26}$$

where Q_c and R_c are symmetric positive (semi) definite matrices, x_k are the states, and u_k is the control input per the control law (e.g., $U_k = K_k x_k$).

With an optimization convergence threshold, ϵ, we can get an optimal solution for this framework with a maximum principle H such that

$$H = (x_k)^T Q_c x_k + (U_k)^T R_c U_k + \lambda(Ax_k + BU_k) \tag{27}$$

where $\lambda_{k+1} - \lambda_k = (\frac{\partial H}{\partial x})^T = Q_c x_k + A^T\lambda_k$ and $U_k = -R_c^{-1}B^T\lambda_k$.

Minimizing (27) is equivalent to minimizing (26). We can see from the above that $(\frac{\partial H}{\partial x})^T = Q_c x_k + A^T\lambda_k$, $(\frac{\partial H}{\partial \lambda})^T = Ax_k + BU_k$, and $\frac{\partial H}{\partial u} = R_c U_k + \lambda^T B$. Therefore, to minimize H, we should find A, B, λ, x_k, and U_k iteratively and solve each of the derivatives.

B. Measurement-Based Optimal Damping Controller Design

Consider two measurements from each generators $\Delta\omega_i$ and ΔV_{Si} with

$$\Delta\omega_i = \omega_i^m - \omega_i^o \tag{28}$$

$$\Delta V_{Si} = V_{Si}^m - V_{Si}^o \tag{29}$$

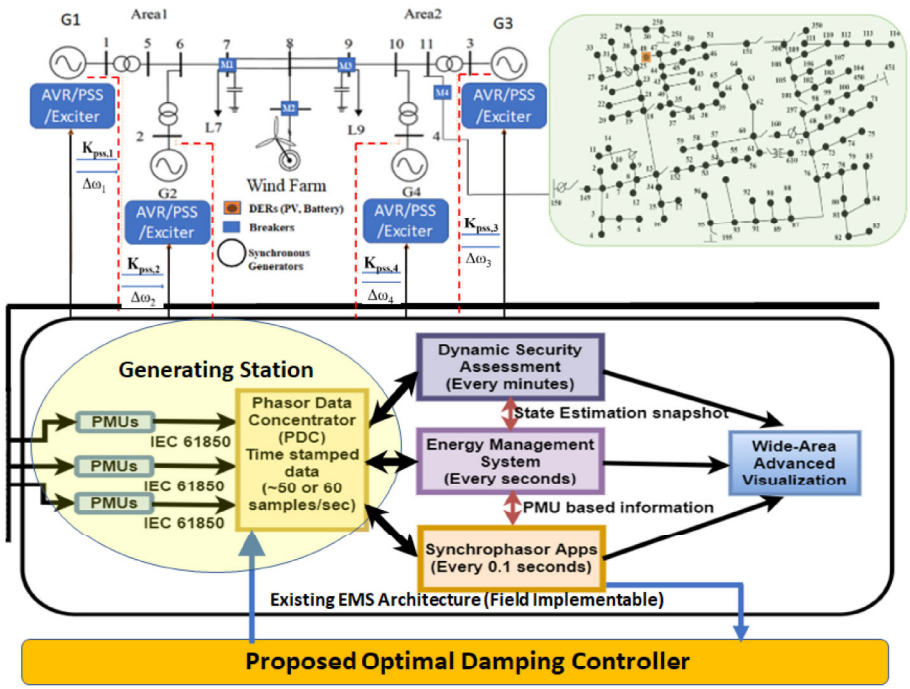

Fig. 3. Field implementation framework of the integrated T&D system with dynamic models of generators and proposed damping controller.

where m and o represent the measured and observed values, respectively. The observed signal is represented as the steady-state moving average value from normal operation conditions.

Consider an optimal controller gain for each generator as $K_{\text{PSS},i}$; then, this gain can be presented from classical equations as

$$K_{\text{PSS},i} = \left\{ \left(\frac{p(\Delta V_{S,i})(1+pT_2)}{1+pT_1} + \frac{(\Delta V_{S,i})(1+pT_2)}{T\omega_i(1+pT_1)} \right) * \frac{1}{p\Delta\omega_i} \right. \tag{30}$$

where $p = \frac{d}{dt}$. With the deviations in speed and voltage represented as in (28) and (29), we have

$$K_{\text{PSS},i} = \left(p(\Delta V_{Si}) + \frac{\Delta V_{Si}}{T\omega_i} \right) * \frac{1}{p\Delta\omega_i} \tag{31}$$

where T is the time constant. To discretize, first, we need to rewrite the deviation of the speed and the control input of the stabilizer per (32) and (33)

$$Y_{2,i} = \Delta\omega_i \tag{32}$$

$$Y_{1,i} = \Delta V_{S,i}. \tag{33}$$

Each of the stabilizer equations then becomes

$$K_{\text{PSS},i} = \left(p(Y_{1,i}) + \frac{Y_{1,i}}{T\omega_i} \right) * \frac{1}{pY_{2,i}}. \tag{34}$$

The discretization of these equations produces the following:

$$K_{\text{PSS},i} = \frac{\Delta Y_{1,i} + bY_{1,i}}{\Delta Y_{2,i}} \tag{35}$$

$$\Delta Y_{2,i} * K_{\text{PSS},i} = \Delta Y_{1,i} + bY_{1,i} \tag{36}$$

where $b = \frac{\Delta t}{\Delta T\omega_1}$.

We can then rewrite (36) as

$$\Delta Y_{1,i} = -bY_{1,i} + K_{\text{PSS},i} * \Delta Y_{2,i}. \tag{37}$$

For multiple generators, (37) can be written as

$$\overbrace{\begin{bmatrix} \Delta Y_{1,i} \\ \vdots \\ \Delta Y_{1,n} \end{bmatrix}}^{x_{k+1}} = -\overbrace{\begin{bmatrix} b_1 \\ \vdots \\ b_n \end{bmatrix}}^{A} \overbrace{\begin{bmatrix} Y_{1,i} \\ \vdots \\ Y_{1,n} \end{bmatrix}}^{x_k=\Delta\omega_i} + \overbrace{[I]}^{B} \overbrace{\begin{bmatrix} K_{\text{PSS},i}\Delta Y_{2,i} \\ \vdots \\ K_{\text{PSS},n}\Delta Y_{2,n} \end{bmatrix}}^{U_k=K_{\text{PSS},i}\Delta V_i}. \tag{38}$$

From the above, it can be seen that with the help of measurements, we can find A, B, x_k, and U_k iteratively. Thus, (28) can be written as $\min_{x_1,\ldots x_T} \Delta\omega_T = \sum_{i=1}^{N} \Delta\omega_i$, where $H = \Delta\omega_T$.

C. Framework to Calculate U_k, λ, and K_{PSS}

For this control application, (38) can be substituted into (28). Derivatives for minimizing (28) can be calculated only if we can find λ and U_k. From (38), it can be seen that

$$U_k^i = \Delta Y_{2,i} * K_{\text{PSS},i}. \tag{39}$$

However, we have to calculate $K_{\text{PSS},i}$ from U_k^i. To solve this, considering the upper and lower limits for $K_{\text{PSS},i}$ as $K_{\text{PSS},i}^U$ and $K_{\text{PSS},i}^L$ and for $\Delta Y_{2,i}$ as $\Delta Y_{2,i}^U$ and $\Delta Y_{2,i}^L$, we can apply four additional McCormick constraints to (28) considering,

$$U_{k+1}^i \geq K_{\text{PSS},i}^L * \Delta Y_{2,i} + K_{\text{PSS},i} * \Delta Y_{2,i}^L - K_{\text{PSS},i}^L * \Delta Y_{2,i}^L \tag{40}$$

$$U_{k+1}^i \geq K_{\text{PSS},i}^U * \Delta Y_{2,i} + K_{\text{PSS},i} * \Delta Y_{2,i}^U - K_{\text{PSS},i}^U * \Delta Y_{2,i}^U \tag{41}$$

$$U_{k+1}^i \leq K_{\text{PSS},i}^U * \Delta Y_{2,i} + K_{\text{PSS},i} * \Delta Y_{2,i}^L - K_{\text{PSS},i}^U * \Delta Y_{2,i}^L \tag{42}$$

$$U_{k+1}^i \leq K_{\text{PSS},i} * \Delta Y_{2,i}{}^U + K_{\text{PSS},i}^L * \Delta Y_{2,i} - K_{\text{PSS},i}^L * \Delta Y_{2,i}^U \tag{43}$$

Algorithm 1: Proposed Adaptive Damping Controller.

Identify all the devices in the network (e.g., generators, wind turbines, and solar PVs) and measurement points.
Initialize the system parameters and K_{pss}, ${K_{pss}}^{U}$, ${K_{pss}}^{L}$, ${\Delta Y_2}^{U}$, ${\Delta Y_2}^{L}$ and ΔY_1 for all the controllable generators.
Compute the speed/frequency deviation signal, $\Delta\omega$, as shown in (28).
Obtain the measure $\Delta\omega$ for each generator, n, and set the value for ϵ.
From step 3, calculate $\Delta\omega_T$, as $\Delta\omega_T = \sum_{i=1}^{N} \Delta\omega_i$.
for $k = 1 : N$ **do**
  while $i \leq n$
  Calculate the A, B, x_k, and U_k using (38) and (39)
  if $\Delta\omega_T \geq \epsilon$ **then**
    Minimize $\Delta\omega_T$ using (27). For this
    Find $K_{pss,i}^{k}$ using (40)-(43)
    Calculate P_k and λ_k using (44)
    Update U_k using (39)
    Calculate $\Delta\omega_T$ using (38)
  else
    if $\Delta\omega_T < \epsilon$ **then**
      $K_{pss,i}^{k} = K_{pss,i}^{k-1}$
    end
  end
end

where i represents damping controller identification number. Therefore, the bilinear terms for the McCormick envelope are $(K_{\text{PSS},i}, Y_{2,i})$. From these constraints, U_k^i can be found from existing and previous values of $K_{\text{PSS},i}$ and $\Delta Y_{2,i}$, where $K_{\text{PSS},i}^{L} = \min_{x_1,\ldots x_T} K_{\text{PSS},i}$ and $\Delta Y_{2,i}^{L} = \min_{x_1,\ldots x_T} \Delta Y_{2,i}$ from the last ten samples. Similarly, we can find $K_{\text{PSS},i}^{U}$ and $\Delta Y_{2,i}^{U}$ with the maximum values of the previous samples.

Finally, λ_k is calculated as

$$\lambda_k = -P_k x_k \tag{44}$$

where P_k is the solution of the Riccati equation for the k-step $= Q_c + K_{\text{PSS},i}^{T} R_c K_{\text{PSS},i} + (A + BK_{\text{PSS},i})^T P_{k-1}(A + BK_{PSS,i})$. For the simulation, we used four PSSs, $i = 1, \ldots, 4$. Using the equations above, the gains of the damping controller, K_{PSS}, are updated at each time interval, based on the deviations seen on the grid. A flowchart of the proposed optimal damping controller algorithm is provided in Fig. 4, and the corresponding optimal adaptive algorithm that dynamically adjusts the gains of the PSS is shown in Algorithm 1.

IV. Results and Discussion

The proposed optimal oscillation damping controller is tested under different scenarios, and the frequency is measured at each of the points, as shown in Fig. 3, to validate the performance. Three test cases scenarios are discussed. Case 1 analyzes the performance of the proposed approach for a fault. Case 2 analyzes the response during dynamic variations of the irradiance profile and the wind speed profile. Case 3 analyzes the performance for a sudden load change. Case 4 shows the operational performance during a harmonic load change.

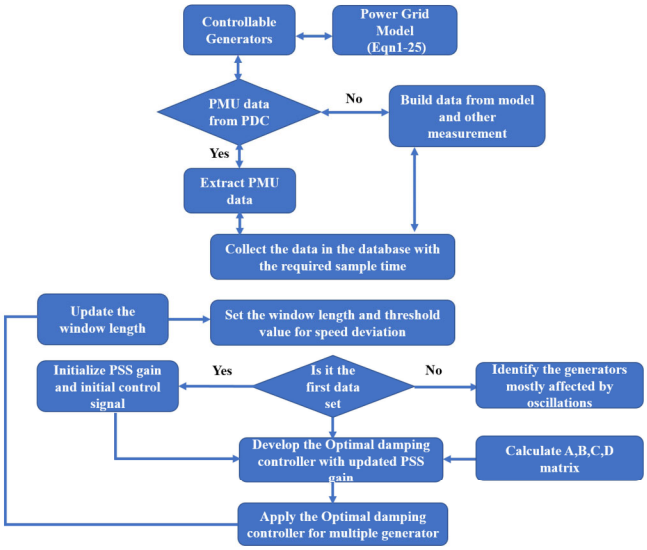

Fig. 4. Flowchart for the proposed optimal damping controller.

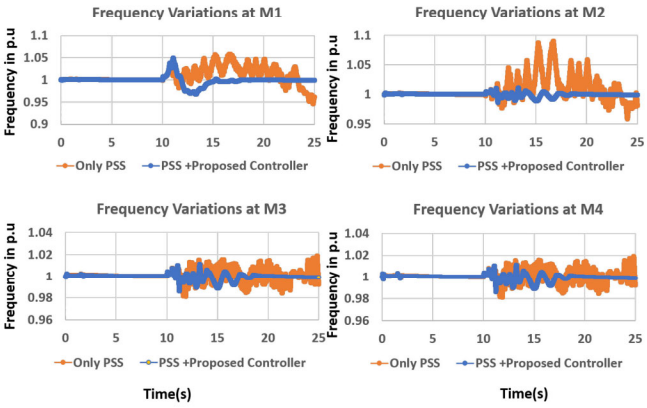

Fig. 5. Case 1A: Grid frequency measurements for fault occurrence at Area 1.

A. Scenario: Fault

In Case 1, the performance of the proposed adaptive PSS architecture is tested for a three-phase-to-ground fault triggered at 10 s at different locations of the test system for a duration of 250 ms.

1) Case 1A: In this case, the performance of the proposed adaptive PSS architecture is tested for a three-phase-to-ground fault triggered at Area 1. The frequency of the generators corresponding to the test scenario is shown in Fig. 5. The results showcase the ability of the proposed controller to provide faster damping of oscillations following a disturbance, as compared with the conventional control approach. The performance of the corresponding dynamic control gain derived by the optimization algorithm for this test case is detailed in Fig. 6. With a fault at Area 1, the contribution of the generators in Area 1 is similar, while the contributions between area generators are different. In addition, the control gains for Area 2 are changing more dynamically, even though the magnitude is lower. Fig. 6 depicts the contribution of the algorithm that dynamically adjusts the control contributions from each of the generators following the event at 10 s.

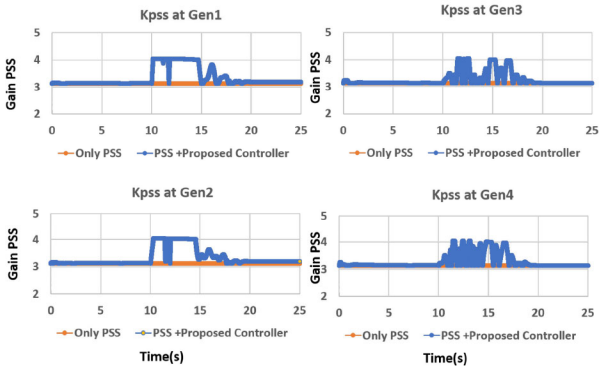

Fig. 6. Case 1A: Dynamically changing gains.

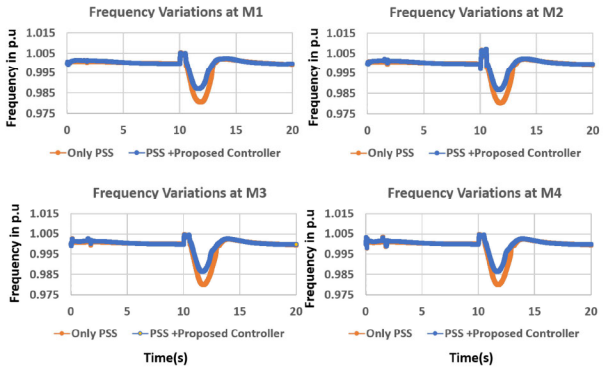

Fig. 7. Case 1B: Grid frequency measurements corresponding to fault occurrence at the tie-line.

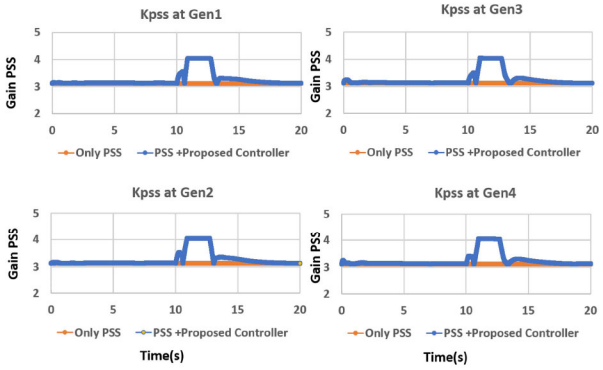

Fig. 8. Case 1B: Dynamically changing gains.

2) Case 1B: In this case, the fault occurrence is on the tie-line. The damping action for all the four measurement points shown in Fig. 3 is depicted in Fig. 7. It can be seen that the damping is similar in all the parts of the grid, which is expected due to the reason that the areas are balanced in power transfer, with an overall improvement of around 1%. The dynamic gains generated by the algorithm in Fig. 8 show that all the generators participate equally toward maintaining the grid frequency when the fault is located at the tie-line.

3) Case 1C: In this case, a fault scenario is developed in the distribution system, and the controller performance for a fault located at the distribution system is detailed in Figs. 9 and 10, respectively. With the proposed control, the contributions from the generator are dynamically adjusted contrary to the conventional PSS, as shown in Fig. 10, resulting in faster damping of oscillations, as shown in Fig. 9.

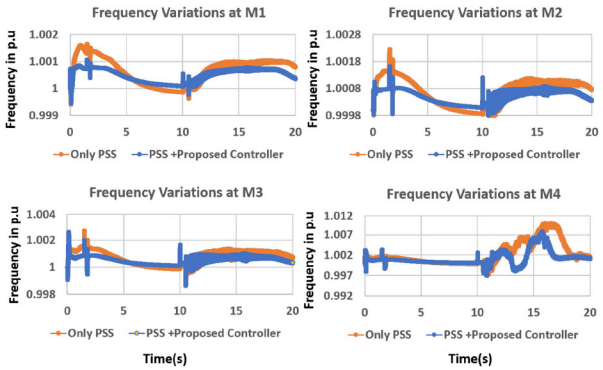

Fig. 9. Case 1C: Grid frequency measurements corresponding to fault occurrence in the distribution system.

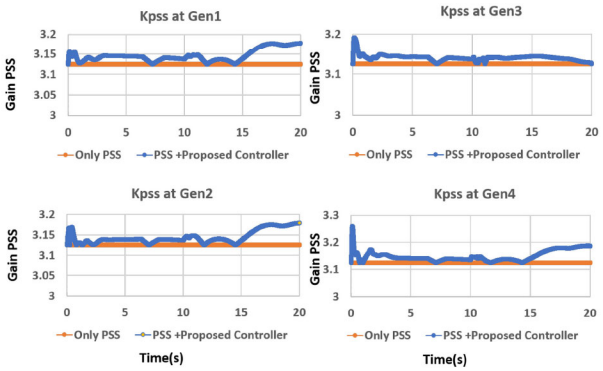

Fig. 10. Case 1C: Dynamically changing gains.

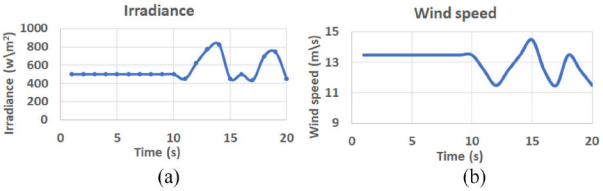

Fig. 11. Case 2: Varying wind speed and irradiance profile.

B. Scenario: Varying Wind Speed and Irradiance Scenario

1) Case 2: In this scenario, the output from solar PVs and the wind turbine is assumed to be varying, due to the variation in irradiance and wind profiles, respectively, as shown in Fig. 11. The corresponding frequency deviations are showcased in Fig. 12, and the controller gains are illustrated in Fig. 13. The results show the ability of the proposed control architecture to tightly maintain the grid frequency to the nominal value, even during highly dynamic input profiles. The larger size of the wind farm shows a much wider low-frequency oscillation in transmission system areas (M_1–M_4). It can be seen that when the PV irradiance is varied (at 10 s), the frequency starts oscillating. With the proposed damping controller, the frequency deviation is close to zero indicating a stable system.

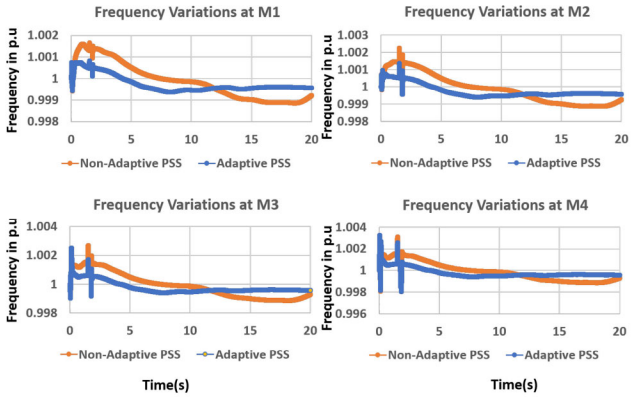

Fig. 12. Case 2: Grid frequency measurements corresponding to change in irradiance and wind profiles.

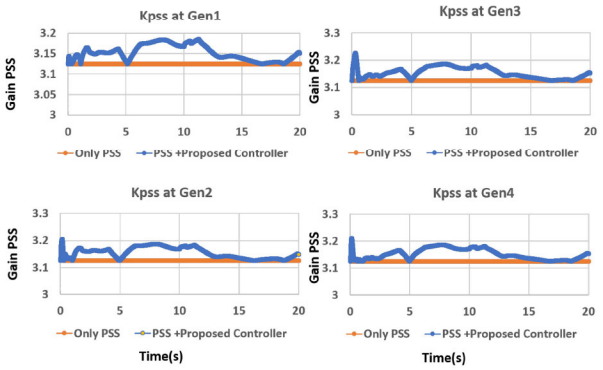

Fig. 13. Case 2: Dynamically changing gains.

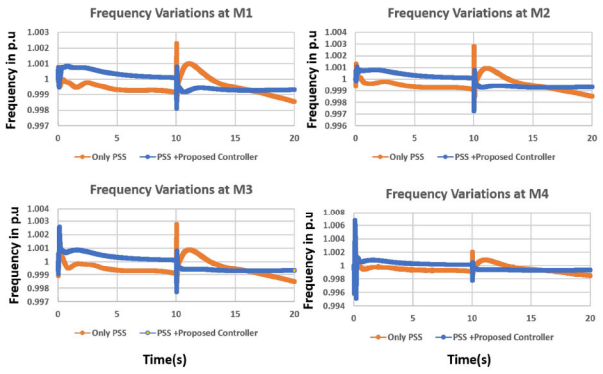

Fig. 14. Case 3: Grid frequency corresponding to sudden load change.

C. Scenario: Sudden Load Change Scenario

1) Case 3: In this scenario, the controller performance was tested for a sudden load change initiated at Area 2. The grid frequency observed at each measurement point is showcased in Fig. 14. The proposed optimization could tightly maintain the frequency around 1 p.u. shortly following the dynamic event. The ability of the proposed optimization algorithm to dynamically adjust the gain following the load change event at 10 s is showcased in Fig. 15. A 47% improvement settling time is observed with the proposed approach compared to the conventional approach.

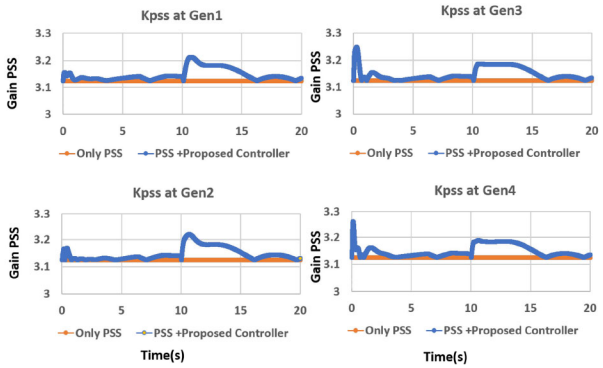

Fig. 15. Case 3: Dynamically changing gains.

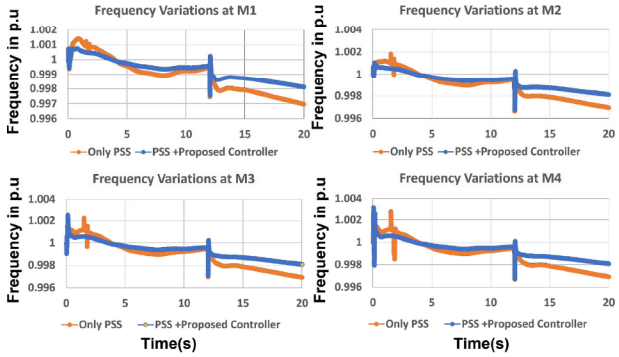

Fig. 16. Case 4: Grid frequency measurements corresponding to harmonic loads.

D. Scenario: Harmonic Loads

1) Case 4: In this case, a harmonic fault scenario has been tested with the proposed controller. To this end, second-order harmonic conditions are created at 12 s during the simulation. The load model is as follows:

$$V_{\text{load}} = V_S - I_1 Z_S \sin(\omega_1 t + \theta_1) - \cdots I_n \sin(n\omega_1 t + \theta_n)(R + jnX). \quad (45)$$

This was initiated by bringing a load online that operates at a different frequency than the grid frequency. The frequency deviation, as observed from the grid, is shown in Fig. 16. It can be seen that at 12 s, the frequency deviations occur due to the switching of these loads. In addition, it can be noted that with the proposed damping controllers, the oscillations in the frequency are reduced. Tables III and IV quantitatively summarize the effect of the proposed controller. Fig. 17 illustrates the dynamically changing gains of the proposed controller.

E. Discussions and Performance Evaluation

As seen from the results provided in Tables II–IV, the performance of our previous damping controller in [28] and the conventional controller (state of the art) is similar. However, with the proposed damping controller, significant improvements in terms of frequency oscillations and settling times have been noticed. PSSs have the advantages of improved damping and stability of the system by providing additional action to the

TABLE II
RELATIVE COMPARISON OF GRID FREQUENCY DEVIATIONS CORRESPONDING TO DIFFERENT TEST CASES

Case	Measurement	Non-Adaptive	Adaptive	% Error
Case 1A	M_1	1.060	0.994	6.23%
	M_2	1.091	0.989	9.35%
	M_3	1.015	1.00	1.48%
	M_4	1.013	1.00	1.28%
Case 2	M_1	0.9985	0.9998	0.13%
	M_2	0.999	0.9995	0.13%
	M_3	0.995	0.999	0.4%
	M_4	0.9985	0.9998	0.14%
Case 3	M_1	1.0012	0.9999	0.13%
	M_2	1.001	0.9998	0.12%
	M_3	1.003	0.998	0.3%
	M_4	1.0015	0.999	0.25%

TABLE III
COMPARISON OF TEST RESULTS WITH AND WITHOUT PROPOSED CONTROL: GRID FREQUENCY

Cases	CC	PC	% Improvement
Fault Case 1	1.0900	0.9895	7.50%
Fault Case 2	1.01	1.001	0.90%
Fault Case 3	0.9751	0.9878	1.28%
Varying Wind-Solar Profile	0.9985	0.9998	0.13%
Load Change	1.0015	0.9998	0.15%
Harmonic load	0.996	0.998	0.21%

Note: CC is conventional control with only PSS. PC is PSS + proposed control.

TABLE IV
COMPARISON OF TEST RESULTS WITH AND WITHOUT PROPOSED CONTROL: SETTLING TIME

Cases	CC	PC	% Improvement
Fault Case 1	17s	25s	15.0%
Fault Case 2	16s	16.8s	4.76%
Fault Case 3	11.8s	14.9s	20.81%
Varying Wind-Solar Profile	12.2s	14.2s	14.08%
Load Change	10.7s	14.4s	25.7%
Harmonic load	12.7s	13.5	5.93%

Note: CC is conventional control with only PSS. PC is PSS + proposed control.

TABLE V
SYSTEM PARAMETERS

Parameter	Value
Wind turbine size	4MVA
Turbine stator voltage	575V
PV farm size	2MVA
Microgrid battery size	1MW
Stator frequency	60Hz
Battery size	800V, 1000AH
Slack generator	900MVA
PV generator 1	900MVA
PV generator 2	900MVA
PV generator 3	900MVA
Mutual inductance L_M	2.9 p.u.
Stator leakage inductance L_{is}	0.1714 p.u.
Rotor resistance R_s	0.0071 p.u.
Rotor leakage inductance L_{ir}	0.1563 p.u.
Number of pole pairs (p)	3
Wind turbine inertia H	0.5s
Synchronous generators line-to-line voltage	4160V$_{LL}$

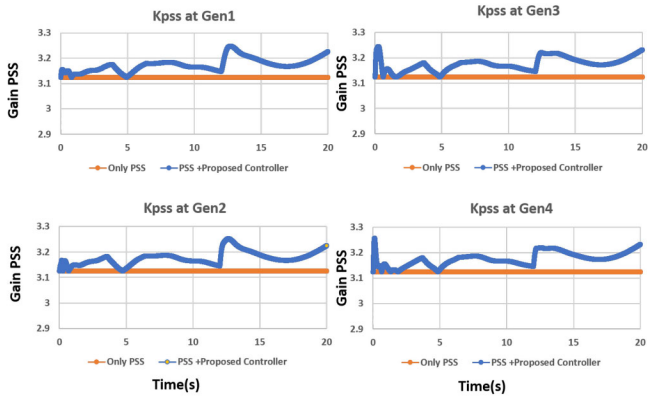

Fig. 17. Case 4: Dynamically changing gains.

excitation controller to damp electromechanical oscillations but have the disadvantages of a longer settling time attributed toward *a priori* modeling and tuning. The main significant advantage of the proposed architecture is that it can be implemented online, autotunes, and can be applied to multiple generators considering both the T&D dynamics.

V. CONCLUSION

In this article, an optimal damping control framework was designed and implemented on an integrated T&D system with bulk power and distributed renewable-based generation. The major contribution and goal were to develop a methodology that can manage the frequency oscillation in an integrated T&D network, with interconnected RERs. The approach relied on an optimal damping control architecture that is adaptive and at the same time optimal. In addition, an optimization technique was implemented to help ensure the optimum performance of the controller, while minimizing the deviation of the grid frequency. The approach was implemented on synchronous generators that can be used to augment the existing stabilizers or other damping controllers. In addition, a field implementation methodology was discussed. The results from simulations on real-life feeders validated the superiority of the proposed control method, as compared with a conventional control approach, to provide an improved grid frequency response for a range of anticipated dynamic conditions (e.g., wind speed variations, faults, and load changes). Overall, a 10% improvement in damping and settling time was observed. Future work will focus on the implementation of the proposed method with the integration of other renewable sources (e.g., energy storage devices, such as supercapacitors, battery banks, and impacts of electric vehicles charging and discharging on the grid) using the proposed approach to keep the grid operation in normal operating conditions. Finally, the hardware implementation of this proposed controller will be performed using the real-time simulator.

REFERENCES

[1] Energy.gov, "Federal agency use of renewable electric energy," Accessed: Dec. 18, 2021. [Online]. Available: https://www.energy.gov/eere/femp/federal-agency-use-renewable-electric-energy

[2] U.S. Environmental Protection Agency, "State renewable energy resources," Accessed: Dec. 18, 2021. [Online]. Available: https://www.epa.gov/statelocalenergy/state-renewable-energy-resources
[3] National Energy Technology Laboratory, "Backup generators (BUGS): The next smart grid peak resource," Nat. Energy Technol. Lab., U.S. Dept. Energy, Tech. Rep. DOE/NETL-2010/1406, 2010.
[4] B. Pokharel, O. Ojo, and A. Balogun, "Standalone operation of a DFIG-based wind turbine system with integrated energy storage," in *Proc. IEEE 6th Int. Symp. Power Electron. Distrib. Gener. Syst.*, 2015, pp. 1–5.
[5] M. Elsisi, M. Aboelela, M. Soliman, and W. Mansour, "Design of optimal model predictive controller for LFC of nonlinear multi-area power system with energy storage devices," *Electr. Power Compon. Syst.*, vol. 46, nos. 11/12, pp. 1300–1311, 2018.
[6] R. Pena, J. C. Clare, and G. M. Asher, "Doubly fed induction generator using back-to-back PWM converters and its application to variable-speed wind-energy generation," *Proc. Inst. Elect. Eng.—Electr. Power Appl.*, vol. 143, no. 3, pp. 231–241, 1996.
[7] M. Yamamoto and O. Motoyoshi, "Active and reactive power control for doubly-fed wound rotor induction generator," *IEEE Trans. Power Electron.*, vol. 6, no. 4, pp. 624–629, Oct. 1991.
[8] H. Tang, W. He, Y. Chi, X. Tian, Y. Li, and Y. Wang, "Impact of grid side converter of DFIG on sub-synchronous oscillation and its damping control," in *Proc. IEEE PES Asia-Pacific Power Energy Eng. Conf.*, 2016, pp. 2127–2130.
[9] R. Maharjan and S. Kamalasadan, "Real-time simulation for active and reactive power control of doubly fed induction generator," in *Proc. North Amer. Power Symp.*, 2013, pp. 1–6.
[10] S. Moghadasi and S. Kamalasadan, "Optimal fast control and scheduling of power distribution system using integrated receding horizon control and convex conic programming," *IEEE Trans. Ind. Appl.*, vol. 52, no. 3, pp. 2596–2606, May/Jun. 2016.
[11] R. Yousefian and S. Kamalasadan, "A Lyapunov function based optimal hybrid power system controller for improved transient stability," *Electr. Power Syst. Res.*, vol. 137, pp. 6–15, 2016.
[12] S. Ghosh and S. Kamalasadan, "An integrated dynamic modeling and adaptive controller approach for flywheel augmented DFIG based wind system," *IEEE Trans. Power Syst.*, vol. 32, no. 3, pp. 2161–2171, May 2017.
[13] S. Abdelrazek and S. Kamalasadan, "A weather-based optimal storage management algorithm for PV capacity firming," *IEEE Trans. Ind. Appl.*, vol. 52, no. 6, pp. 5175–5184, Nov./Dec. 2016.
[14] M. Ramirez-Gonzalez and O. P. Malik, "Power system stabilizer design using an online adaptive neurofuzzy controller with adaptive input link weights," *IEEE Trans. Energy Convers.*, vol. 23, no. 3, pp. 914–922, Sep. 2008.
[15] J. A. O. Lala and C. F. Gallardo, "Adaptive tuning of power system stabilizer using a damping control strategy considering stochastic time delay," *IEEE Access*, vol. 8, pp. 124254–124264, 2020.
[16] P. Zhao and O. P. Malik, "Design of an adaptive PSS based on recurrent adaptive control theory," *IEEE Trans. Energy Convers.*, vol. 24, no. 4, pp. 884–892, Dec. 2009.
[17] J. Zhang, C. Y. Chung, C. Lu, K. Men, and L. Tu, "A novel adaptive wide area PSS based on output-only modal analysis," *IEEE Trans. Power Syst.*, vol. 30, no. 5, pp. 2633–2642, Sep. 2015.
[18] L. Zacharia, M. Asprou, and E. Kyriakides, "Wide area control of governors and power system stabilizers with an adaptive tuning of coordination signals," *IEEE Open Access J. Power Energy*, vol. 7, pp. 70–81, 2020.
[19] S. R. Paital, P. K. Ray, and A. Mohanty, "Firefly-swarm optimized fuzzy adaptive PSS in power system for transient stability enhancement," in *Proc. Prog. Electromagn. Res. Symp.*, 2017, pp. 1969–1976.
[20] S. Kamel, B. Ziyad, H. M. Naguib, A. Mouloud, and R. Mohamed, "An indirect adaptive type-2 fuzzy sliding mode PSS design to damp power system oscillations," in *Proc. 7th Int. Conf. Model., Identif. Control*, 2015, pp. 1–6.
[21] F. Jamsheed and S. J. Iqbal, "Design of an adaptive power system stabilizer using robust system-response prediction," in *Proc. IEEE Int. Conf. Power Electron., Smart Grid Renewable Energy*, 2020, pp. 1–6.
[22] M. Mahdavian, A. Movahedi, G. Shahgholian, and M. Janghorbani, "Coordinated control of PSS and variable impedance devices by using avurpso to enhance the stability in power system," in *Proc. 14th Int. Conf. Elect. Eng./Electron. Comput., Telecommun. Inf. Technol.*, 2017, pp. 407–410.
[23] X. Xie, "PSS control of multi machine power system using reinforcement learning," in *Proc. 5th Int. Conf. Robot. Autom. Sci.*, 2021, pp. 132–135.
[24] S. Kamalasadan and A. A. Ghandakly, "A neural network parallel adaptive controller for fighter aircraft pitch-rate tracking," *IEEE Trans. Instrum. Meas.*, vol. 60, no. 1, pp. 258–267, Jan. 2011.
[25] S. Kamalasadan, "A new intelligent controller for the precision tracking of permanent magnet stepper motor," in *Proc. IEEE Power Eng. Soc. Gen. Meeting*, 2007, pp. 1–7.
[26] S. Kamalasadan and A. A. Ghandakly, "Multiple fuzzy reference model adaptive controller design for pitch-rate tracking," *IEEE Trans. Instrum. Meas.*, vol. 56, no. 5, pp. 1797–1808, Oct. 2007.
[27] S. Kamalasadan and A. A. Ghandakly, "A neural network based intelligent model reference adaptive controller," in *Proc. IEEE Int. Conf. Comput. Intell. Meas. Syst. Appl.*, 2004, pp. 174–179.
[28] O. Ogundairo, A. R. Nair, M. Smith, and S. Kamalasadan, "Online adaptive damping controller architecture for wind integrated power grid," in *Proc. IEEE Int. Conf. Power Electron., Drives Energy Syst.*, 2020, pp. 1–6.

Olalekan Ogundairo (Student Member, IEEE) received the B.Sc. degree in electrical and electronic engineering from Obafemi Awolowo University, Ile-Ife, Osun, Nigeria, in 2016. He is currently working toward the Ph.D. degree in electrical engineering with the University of North Carolina at Charlotte, Charlotte, NC, USA.

His current research interests include distributed energy resources grid integration, management control, and optimization, modeling, and analysis of weak grid, power system stability, and control.

Sukumar Kamalasadan (Senior Member, IEEE) received the B.Tech. degree in electrical and electronics from the University of Calicut, Thenhipalam, India, in 1991, the M.Eng. degree in electrical power systems management from the Asian Institute of Technology, Bangkok, Thailand, in 1999, and the Ph.D. degree in electrical engineering from the University of Toledo, Toledo, OH, USA, in 2004.

He is currently a Professor with the Department of Electrical and Computer Engineering, University of North Carolina at Charlotte, Charlotte, NC, USA. His research interests include intelligent and autonomous control, power systems dynamics, stability and control, smart grid, microgrid, and real-time optimization and control of power system.

Dr. Kamalasadan was the recipient of several awards including the NSF CAREER Award and IEEE Best Paper Award.

Anuprabha R. Nair (Student Member, IEEE) received the B.Tech. degree from Calicut University, Thenhipalam, India, in 2010 and the M.S. degree from Purdue University, West Lafayette, IN, USA, in 2016, both in electrical engineering. Since 2017, he has been working toward the Ph.D. degree in electrical engineering with the Department of Electrical and Computer Engineering, University of North Carolina at Charlotte, Charlotte, NC, USA.

Her research interests include renewable energy integration and stability, wind energy conversion system, modeling and analysis of weak grid, power system stability, and control, Integration of distributed energy resources, and contribution to power system stability.

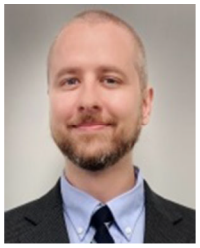

Michael Smith (Member, IEEE) receive the B.S. degree in mechanical engineering technology, the M.S. degree in mechanical engineering, the second M.S. degree in electrical engineering, and the Ph.D. degree in electrical engineering from the University of North Carolina at Charlotte, Charlotte, NC, USA, in 2005, 2008, 2012, and 2015, respectively.

He is currently an Assistant Professor with the Department of Engineering Technology and Construction Management, University of North Carolina at Charlotte. His research interests include real-time process modeling, stability and control, adaptive control, process automation and optimization, data analytics, applied energy, and electromechanical systems.